JOURNAL OF PROPULSION AND POWER
Vol. 22, No. 3, May–June 2006

Numerical Modeling of a Pulsed Electromagnetic Plasma Thruster Experiment

J. T. Cassibry*
University of Alabama in Huntsville, Huntsville, Alabama 35899
Y. C. Francis Thio†
U.S. Department of Energy, Germantown, Maryland 20874
T. E. Markusic‡
NASA Marshall Space Flight Center, Huntsville, Alabama 35812
and
S. T. Wu§
University of Alabama in Huntsville, Huntsville, Alabama 35899

We assessed the behavior and capabilities of a two-dimensional magnetohydrodynamic modeling code with a new tabular equation of state model for high-power pulsed plasma thrusters. The numerical results enabled detailed interpretation of the experimental data from a ∼10-kJ pulsed coaxial plasma accelerator with ablative breech insulator polytetrafluoroethylene. Our analysis showed that the initial conditions and ablation rate are critical to the behavior of the current sheet evolution in the numerical model. Qualitative agreement was obtained between the two-dimensional numerical model and experimental results, but there were significant quantitative discrepancies. The two-dimensional model indicates that some of the current remains trapped near the breech, because of the ablation of material off the breech boundary, which appears to be supported by the experimental data. The sensitivity of the model to initial prefill density (small in comparison with the ablated mass) and ablation rate suggests that future modeling efforts involving high-power ablative fed pulsed plasma thrusters using the approach discussed in the paper should include a first-principles ablation model, together with density, temperature, and ablation rate estimates from the experimental apparatus.

Nomenclature

B	=	magnetic field, T
E_0	=	energy level of operation, J
h	=	heat of vaporization, J/kg
I	=	current, A
k	=	Boltzmann's constant, J/K
n	=	density, m^{-3}
P	=	pressure, Pa
R	=	gas constant
R_e^G	=	gasdynamic Reynolds number
R_e^M	=	magnetic Reynolds number
r	=	radial coordinate, m
T	=	temperature, K
t	=	time, s
z	=	axial coordinate, m
δ	=	diffusion scale length, m
ε	=	error
μ	=	viscosity coefficient
μ_0	=	magnetic permeability, H/m
ρ	=	mass density, kg/m^3
σ	=	plasma conductivity, $\Omega \cdot m^{-1}$
τ	=	collision time, s

Subscripts

eff	=	effective
exp	=	experiment
i	=	ion
max	=	maximum value
n	=	probe number
run	=	numerical simulation
tot	=	total
θ	=	azimuthal coordinate
0	=	reference value

Received 21 February 2005; revision received 15 August 2005; accepted for publication 16 August 2005.

*Assistant Research Professor, Propulsion Research Center, Department of Mechanical and Aerospace Engineering, Technology Hall S-227. Member AIAA.

†Program Manager, Office of Fusion Energy Sciences, SC-55, 19901 Germantown Road.

‡Research Engineer, Propulsion Research Center, Building 4205. Member AIAA.

§Director, Center for Space Plasma and Aeronomy Research and Distinguished Professor, Mechanical and Aerospace Engineering Department, Technology Hall N272B. Fellow AIAA.

Introduction

DETAILED magnetoplasmadynamic modeling and comparison with experimental results provide a means to understand complexities in pulsed plasma thrusters (PPT) and hence to improve their performance. Research and development of pulsed plasma thrusters has been conducted for more than 40 years.[1–3] However, computers have only been powerful enough in the past 20 years or so to enable magnetohydrodynamic (MHD) modeling using two or more spatial dimensions.

Keefer and Rhodes[4] have recently used an MHD code[5] to model plasma thrusters. Using the Two-Dimensional Multiblock Arbitrary Coordinate Hydromagnetic (MACH2) Code,[5–8] they showed that the relative importance of electrothermal and electromagnetic acceleration mechanisms depends on the specific thruster parameters, especially the total mass injected. For higher mass injection, a large portion of the total current remains attached at the breech, so that much of the acceleration is electrothermal. Rhodes and Keefer used MACH2 to model cableguns,[9] in which cathode and insulator materials and propellants were varied. They obtained reasonable estimates of plasma plume properties that would be difficult to

determine experimentally, such as spatial flow details including electron number density and the plume width and temporal distribution of propellant loss.

In PPTs, a large fraction of the propellant mass is poorly utilized because of late-time ablation, reducing the effective specific impulse of the device. Thus, mass utilization efficiency is an important issue for this class of thrusters.[10] Turchi and coworkers[3,11,12] have sought to understand the physics of PPT mass utilization through numerical modeling in order to improve thruster performance. Turchi developed a one-dimensional MHD model; the results showed that an inductively driven circuit, such as a resistive-inductive-capacitive (RLC) circuit, crowbarred near peak current, with a prolonged current pulse, can increase the fraction of mass accelerated electromagnetically.[3] Using MACH2, Turchi et al. found that late time ablation and macroparticle production consist of a significant fraction of the propellant lost.[11,12] A recent study was made by Shen et al.[13] They were able to obtain an analytical solution for the snowplow model[14] under the assumption that the maximum gun impedance was an order of magnitude smaller than the circuit resistance. With this model, they achieved qualitative agreement with experimentally measured plasma velocity. Earlier work of this type includes that of Andrenucci et al.[15]

Numerical modeling of plasma thrusters, with emphasis on the magnetoplasmadynamic (MPD) thruster, has been summarized by both Mikellides[16] and Sankaran et al.[17,18] Mikellides applied MACH2 to model related (but quasi-steady-state devices) MPD thrusters.[16,19–22] The code was successful in capturing experimental trends in thrust, voltage, and current distribution.[20,22] Mikellides et al.[23] later utilized MACH2 in the design of a high-power MPD thruster as a plasma source. Sankaran developed a new two-dimensional MHD code for modeling plasma thrusters.[17,18] This model has been validated with measured current density patterns in an MPD thruster.

The coaxial pulsed plasma accelerator we discuss in this work is an unsteady device similar in geometry to that of self-field MPD thrusters but with quite different physical behavior as a result of the time-dependent nature of the current pulse and typically much higher R_e^M. This device has an advantage over MPD thrusters in that the plasma velocity is (apparently) not limited to a factor of the critical Alfven speed, such as has been demonstrated by Markusic et al.[24] and Cheng,[25] for example. It is similar to ablative-fed[1] and gas-fed[26] PPTs that have been studied, but it is both much larger in physical scale and energy.

Despite a recent wealth of work in MHD modeling, there has been very little in the way of comparison with experimental data from coaxial pulsed plasma accelerators. In this work, we compare two-dimensional numerical results using MACH2,[5–8] with magnetic field and light pipe probe diagnostics. The main objectives are to assess and validate the capabilities of MACH2 in modeling high-power-density PPTs, what might be required in the way of additional development of the code, and to add the experience to the existing application database of the code. This work can assist future researchers who use MACH2 to perform analyses of the behavior of pulsed plasma accelerators of similar sizes and energy levels.[27] We concentrate our discussion on the first-quarter-period circuit pulse, which is the time in which the plasma reaches the accelerator exit. We first briefly describe the experimental device. We then present the computational tools used to model the device, which are based on the fluid approach. We compare numerical and experimental magnetic field probe measurements and correlate the time-of-flight velocity measurements with light pipe probe data in order to gain valuable insights into the dynamics of the accelerated plasma. We then discuss the two-dimensional plasma and current sheet evolution in more detail.

Brief Description of the Experiment

The numerical model discussed here is based on a recent set of experiments performed using a coaxial plasma accelerator, Pulsed Electromagnetic Plasma Accelerator-0 (PEPA-0). More details of that experiment are reported elsewhere.[27–29] Although the original intent of the accelerator was to serve as an electrical load in the development of the pulsed power laboratory and not intended to be a high-performance thruster, the testing of the system and the accelerator provided an invaluable opportunity to attempt two-dimensional MHD modeling of the accelerator behavior with an ablative breech boundary. Although numerous dielectrics have been investigated as propellant sources for breech-fed ablative thrusters,[30,31] Polytetrafluoroethylene (PTFE) was chosen for its low surface charring characteristics, popularity of its use in PPTs,[1] and low cost.

Table 1 Positions of the light pipe probes as measured from the trigger

Probe name	Position, cm
LP1	2.5
LP2	7.6
LP3	17.8
LP4	27.9
LP5	38.1
LP8	53.3
LP10	132.1

Table 2 Positions of the $\dot{B}$ probes as measured from the trigger

Probe name	Position, cm
$\dot{B}_{1\theta}$	5.1
$\dot{B}_{2\theta}$	12.7
$\dot{B}_{3\theta}$	22.9
$\dot{B}_{5\theta}$	33.0
$\dot{B}_{6\theta}$	43.2

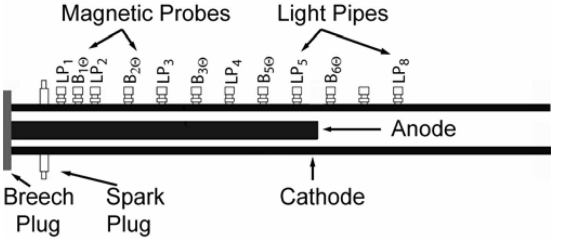

Fig. 1 Illustration of PEPA-0 with salient features and diagnostics identified. The inner and outer electrodes are the anode and cathode, respectively.

PEPA-0 consists of a pair of coaxial cylindrical electrodes. The inner electrode (anode) has a diameter of 2.67 cm (1.05 in.) and is 0.464 m (18.25 in.) long measured from the breech plug (Fig. 1). The outer electrode (cathode) has a diameter of 5.40 cm (2.125 in.) and is 0.813 m (32.0 in.) long measured from the same breech plug. The plasma gun is connected to an RLC circuit consisting of two parallel 330-μF capacitors with a parasitic transmission line inductance and resistance of 230 nH and 5 mΩ, respectively. There are no external switches. The capacitors are rated for 10-kV maximum voltage, though testing was conducted with the voltage below 6 kV.

At 7.0 cm (2.75 in.) from the breech plug is a set of six ordinary automobile spark plugs. These spark plugs are used for initiating the capacitive discharge. The gun is equipped with a number of diagnostic ports (holes) along its length (Fig. 1). They have been used for holding light pipes and magnetic ($\dot{B}$) probes. A set of six light pipes for in-bore optical emission monitoring and five magnetic probes were used in the series of tests completed. The light pipe and $\dot{B}$ probe positions are summarized in Tables 1 and 2, respectively. A series of experimental runs was performed with an initial charging voltage of 5400 V, or approximately 9600 J per shot. They are data from this series that we compare with our numerical model.

Numerical Model of the Electromagnetic Accelerator

Based on its history of success in modeling a wide variety of physics problems,[4,9,32–37] the principal tool for modeling and interpreting the experimental results presented here was the

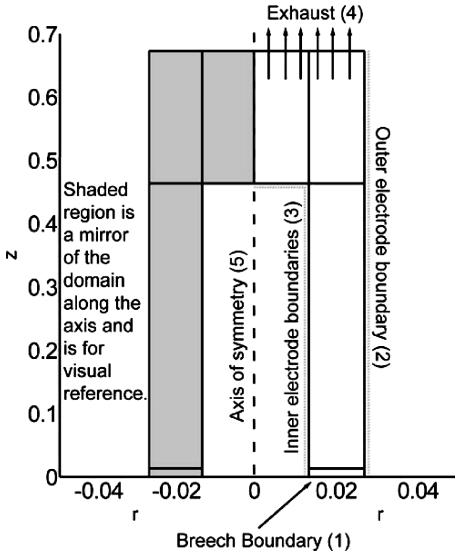

Fig. 2 Computational domain for PEPA-0.

two-dimensional MHD code MACH2[5–8] with some modifications to accommodate the real-gas effects for PTFE, which will be discussed later. MACH2 is a two-and-one-half-dimensional multiblock, arbitrary Lagrangian Eulerian, resistive magnetohydrodynamic (MHD) code that carries all three spatial components of vectors, but allows no quantity to depend on the coordinate that is normal to the computational plane.[8] MACH2 solves the mass, momentum, electron energy, ion energy, radiation energy density, and magnetic induction equations in a fractional time-split manner for the flow variables. The equations are closed with an ideal-gas equation of state, Braginskii thermal conductivity for components perpendicular and parallel to the magnetic field[38] and Spitzer resistivity.[39] MACH2 was run on an IBM RS6000 workstation running AIX version 4.3, for all results reported in this work.

The computational domain is chosen according to the experiment as shown in Fig. 2, along the right-hand side of the axis of symmetry, boundary (5). The domain is mirrored along the axis as shown for illustrative purposes. In Fig. 2 the radial and axial coordinates are r and z, respectively. The axes are not to scale. The plasma flow is assumed to be axisymmetric. The physics in the MACH2 model include thermal diffusion, magnetic field diffusion, an equilibrium equation of state model for PTFE, and a self-consistent RLC circuit model set to the experimental operating conditions of PEPA-0 for $E_0 = 9600$ J (5400 V, 660-μF capacitance, 180-nH external inductance, and 1.0-mΩ external resistance). The domain contained an initial global mass density of 1.5×10^{-4} kg/m^3. It must be emphasized that experimentally the accelerator was operated with essentially no prefilled gas, in that the accelerator was flushed with helium mixed with a small amount of argon (0.46%) and evacuated down to a pressure of less than 10 mt orr typically at room temperature. The prefill density in the main acceleration region used in the computation is a numerical artifact to simulate the estimated mass entrained by the plasma during the experiment produced by electrode erosion.[26] We investigated other values for the prefill densities, and those results are presented later in the text. The initial global temperature was 0.025 eV (270 K).

The magnetic field probes were the primary diagnostic tool used to compare with the numerical model; thus, computational grid cell sizes must be sufficiently small to resolve magnetic field scale lengths of interest. A local change in the magnetic field is propagated in the plasma by magnetic diffusion and displacement current. In terms of the magnetic diffusion, in a time interval Δt the field disturbance diffuses to a depth

$$\delta = \sqrt{\pi \Delta t / \mu_0 \sigma} \tag{1}$$

To resolve local magnetic field changes within a time interval Δt, the cell dimension should be less than δ. In our model, the temperature in the main accelerator section is typically 2.5 eV, and the number density is $\sim 10^{23}$ #/m^3. The Spitzer conductivity in this case is of the order $10^4(\Omega \cdot \mathrm{m})^{-1}$. In this paper, we attempt to compare experimental data with our numerical modeling and resolve magnetic field changes to within 0.5 μs, which gives a diffusion length of about 11 mm. Accordingly, we have chosen the cell dimensions that vary from 0.6 to 3.7 mm. In the axial direction (parallel to the gun axis), the magnetic field gradient is governed by spatial scale of the magnetic field diffusion. This is treated in the preceding discussion. In the radial direction, the spatial scale for the magnetic field distribution is $\sim |B/(\partial B/\partial r)| = r$. In the radial direction, the chosen cell size was 1/8 of this spatial scale and should therefore be adequate in modeling the effects caused by this distribution. The computational mesh consisted of eight subdivisions across the radial gap between the electrodes and 200 along the axis. In addition, the block downstream of the inner electrode was an 8×8 mesh. We doubled the mesh resolution in some test runs as a check; however, this did not significantly affect the current sheet structure or flow dynamics.

The wide range of densities and temperatures that exist in a high-power coaxial plasma accelerator require accounting for multiple levels of ionization. In addition, PTFE requires accounting for dissociation of the molecular species and rotational and vibrational excitation to accurately model the internal energy at given density and temperature. A tabular equation of state model for PTFE was used for the thermodynamic variables including temperature, pressure, specific heat, polytropic index, and species mole fraction as a function of density and specific internal energy. A separate code, Aurora, was used to generate the table and is discussed in some detail elsewhere.[27] This model assumes thermal, chemical, and local thermodynamic equilibrium. The nonlinear system of equations consisting of mass action and atomic conservation laws was solved in that code using a modified fixed-point method algorithm for the equilibrium number density distribution of the species at a given density and specific internal energy for the following 21 species: C_2F_4, CF_2, CF, C, C^+, C^{2+}, C^{3+}, C^{4+}, C^{5+}, C^{6+}, F, F^+, F^{2+}, F^{3+}, F^{4+}, F^{5+}, F^{6+}, F^{7+}, F^{8+}, F^{9+}, and e^-. With the equilibrium composition and the partition functions, the calculation of the thermodynamic quantities is straightforward, and the equations can be found in a number of sources, Vincenti and Kruger,[40] for example.

The viscous boundary layer at all material walls is ignored; thus, all wall boundaries are treated as freeslip velocity conditions. Using the Braginskii formula,[38] the scalar ion viscosity coefficient is

$$\mu_i = 0.96 n k T \tau_{ii} \tag{2}$$

For $T \sim 35{,}000$ K (3 eV) and $n \sim 10^{23}$ m^{-3}, typical values in the experiment and numerical model, the ion collision time is about 1 ns for the fully ionized carbon and fluorine atoms of which PTFE primarily consists, corresponding to a viscosity of about 5×10^{-5} kg/m $\cdot$ s and R_e^G of $\sim$40,000 using the gap between the electrodes as the scale length of interest. We expect that viscous effects could lead to propellant losses at the wall and viscous dissipation, which can accelerate electrode degradation. However, a viscous calculation would require significantly higher grid resolution in order to resolve the small-scale boundary layer near the electrode walls and was beyond the scope of the present study.

The breech boundary (1) in Fig. 2 ablates PTFE. If the temperature at the insulator (PTFE) surface is below its critical point of the phase transformation, then the ablated material would first appear at the surface as a saturated vapor. The pressure in the first row of computational cells is used to calculate the equilibrium vaporization temperature and density of the saturated vapor by interpolating between points of equilibrium vaporization data, which are given in Table 3. The data were calculated with the expression

$$P = P_0 e^{(h_{\mathrm{eff}}/R)(1/T_n - 1/T)} \tag{3}$$

This expression is obtained from the Clausius–Clayperon equation from the second law of thermodynamics for the phase change of a material. We used an effective enthalpy of vaporization h_{eff} of approximately 1.768×10^6 J/kg, within the range suggested by

Table 3 Vaporization data for PTFE

P_{vap}, Pa	T_{vap}, K	ρ_{vap}, kg/m^3
1.218×10^{-11}	350	4.353×10^{-16}
1.003×10^{-03}	500	2.509×10^{-8}
$1.834 \times 10^{+01}$	650	3.530×10^{-4}
$8.460 \times 10^{+03}$	800	1.323×10^{-1}
$5.624 \times 10^{+05}$	950	7.405×10^{0}
$1.190 \times 10^{+07}$	1100	$1.353 \times 10^{+2}$
$1.211 \times 10^{+08}$	1250	$1.212 \times 10^{+3}$

Wentink.[41] We used 83.1 J/kg · K for the PTFE gas constant, the approximate value for the C_2F_4 monomer in the vapor state. The reference values for temperature and pressure were 748 K and 1333.2 Pa, respectively, and were also obtained from Wentink.[41] In the finite volume discretization of MACH2, the velocity is determined at the grid cell nodes (corners), and the pressure is cell centered. At the external ghost cell nodes, the velocity, as has been stated, is set to freeslip, making the normal component of velocity at the ablation boundary zero. The total (thermodynamic + magnetic) pressure gradient accelerates the ablated material across the cell faces between the ghost cells and the computational domain. Further discussion of the ablation model is given in the section where the modeling results are presented and discussed. Along the top face of domain, exhaust boundary (4) is a hydrodynamic continuity boundary. No spatial gradients are allowed across this boundary by copying the flow variables from the last row of computational cells to the ghost cells. The plasma moves freely across boundary 4. All other external boundaries (2, 3, and 5) are treated as walls with the freeslip velocity condition, and there are no constraints imposed on the internal block boundaries.

Along the faces adjacent to the inner electrode and the right boundary of the domain, boundaries (3) and (2), the walls are treated as a conductor. The product of the radial coordinate and the azimuthal magnetic field B_θ is treated as a constant along these boundaries, which forces the current density to be tangential to the surface. This assumption has been tested in cases where electrodes were included in the computation with a resistivity comparable to that of copper, and it shows that the current density was always tangential to the electrode wall adjacent to the interior of the accelerator. The skin depth was smaller than the grid resolution of 1 mm, and so no current diffused into the electrode beyond the first row of cells. Thus, no cases with the electrodes included in the computation are reported here, as they have not affected the results significantly. Along the exhaust boundary, B_θ was simply copied into the ghost cells, like the continuity boundary condition imposed for the thermodynamic variables.

The breech boundary is treated as an insulator and is attached to a self-consistent circuit model. The equation for the magnetic field along this boundary is derived from Ampere's law, where the displacement current is neglected.[6] For a coaxial geometry, this equation is

$$B_\theta = \mu_0 I / 2\pi r \tag{4}$$

Equation (4) holds so long as the capacitive effect of the coaxial electrodes can be ignored. This is a frequent assumption made in these devices. The circuit model is coupled to the accelerator by calculating the voltage drop across the insulator boundary.

During the initiation phase of the circuit, the particle mean free path is large in comparison with the width between the electrodes. Thus, the continuum approach is inadequate for a fluid model such as MACH2. A study of the initiation phase physics requires a coupled particle kinetic and circuit model, which was done by Cassibry[27] and Thio et al.[28,29] To develop the initiation model, we used the prefill conditions of the plasma thruster and pulse shape of the circuit from a shot typical of conditions in the experiment. We calculated the collision mean free path as a function of time, using estimates of the density and temperature. Based on the theoretical model, we showed that the transition to more fluid-like behavior begins at about 100 ns. Further details of that model and the initiation physics are discussed elsewhere.[27–29] For simplicity, we begin the two-dimensional MACH2 simulation at $t = 0$, using the quiescent cold-gas conditions prior to initiation. In the computation, because the mass of the "prefill" and the ablation of the breech constrain the macrodynamics of the plasma, we do not expect the initiation process to affect significantly the modeling results in late time.

Modeling Results

Comparisons of Two-Dimensional Simulations with Experiments

$\dot{B}$ and light pipe probes were among the diagnostics used in the series of experiments with PEPA-0. The probe stations are as shown in Fig. 1. The current from the $\dot{B}_{1\theta}$ signal, the probe closest to the trigger, is compared for a typical shot and the two-dimensional numerical model, Fig. 3, with error bars shown for reference. We used Eq. (2.19) in Coleman and Steele[42] to determine the random uncertainty (repeatability within 95% confidence limit) on the measured current, which was about 5% of the peak current for 16 shots taken at the same experimental conditions. The measured current rises sharply from about 1 μs and peaks at 17.9 μs at 157 kA. Current reversal occurs at 40.6 μs. The current from the corresponding virtual probe peaks at 18.7 μs at 141 kA. Current reversal occurs at 39.0 μs, close to that measured in the experiment. The current determined in the model is generally lower than the measured one and is outside the repeatability range, indicating that more magnetic flux is propagating downstream of the $\dot{B}_{1\theta}$ probe. There is about a 10% difference between the arrival time of the current sheet in the measured and numerical results, compared to the transit time from the breech to the exit. It is possible that the model overpredicts the electrical conductivity at the breech boundary. This would slow the propagation of the magnetic field into the body of the plasma and cause the discrepancy between the measurement and model. Another possibility is that the ablation rate is overestimated, delivering too much mass to the breech region and consequently reducing the acceleration of the plasma. This will be treated later in this paper.

Scaled $\dot{B}$ probe currents (scale factor is 10^{-6}) are shown as a function of position in Fig. 4 with corresponding repeatability bars. An illustration of the plasma accelerator is included to indicate the relative positions of the magnetic field measurements along the y axis. The results from MACH2 are overlaid with the experimental data. Figure 5 clearly indicates a current sheet propagating downstream. The numerical results were able to capture qualitatively both the advancement of the current sheet and the trapping of flux near the breech, caused by the ablating breech boundary. The general trend is that the model overpredicts the magnetic field strength as it propagates downstream from the first probe. This suggests that significant current is getting trapped between the first and second probes in the experiment because of arcing or resistive dissipation; nevertheless, the model was successful in capturing quantitatively the magnetic field strengths between 10 to 20 μs for the last two probes (Fig. 4).

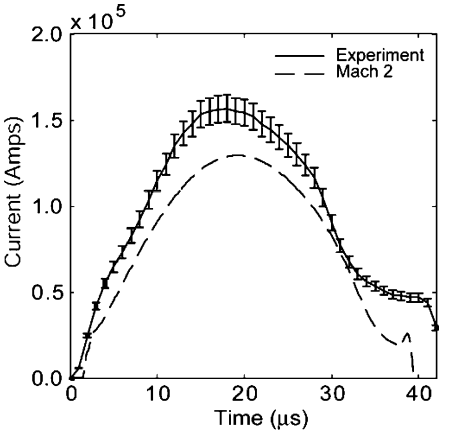

Fig. 3 Comparison of $\dot{B}$ probe data from experiment and MACH2 results: —— and – – – represent experimental and MACH2 data, respectively.

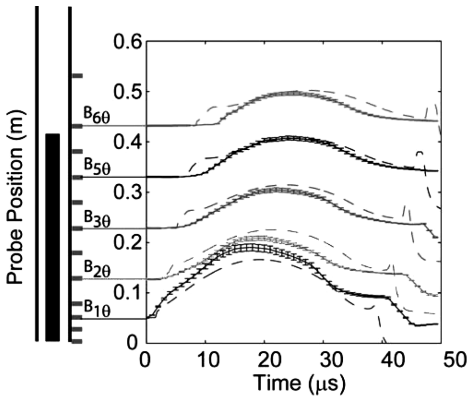

Fig. 4 Comparison of experimental and MACH2 $\dot{B}$ current as a function of probe position: —— and – – – represent experimental and MACH2 data, respectively. Error bars are given for the experimental data.

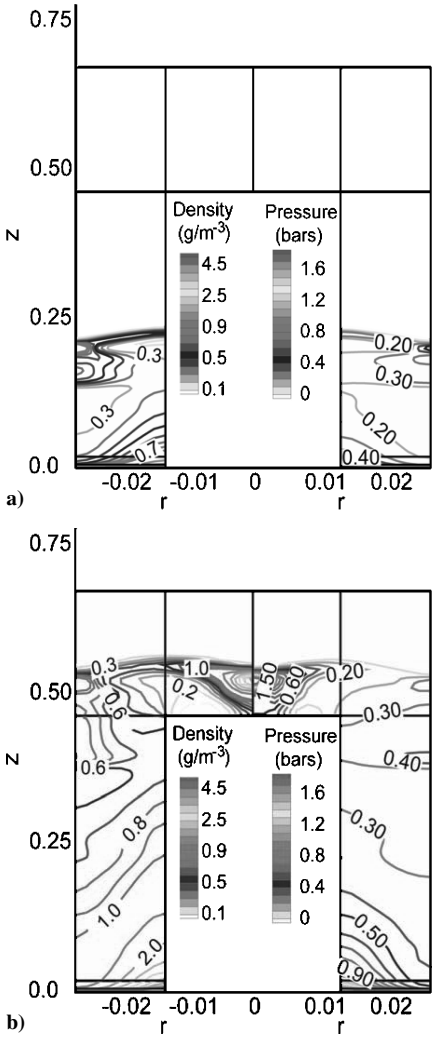

Fig. 5 Simulated density (left) and pressure (right) contours at a) 7.5 μs and b) 15 μs.

From Fig. 4 one can estimate the velocity by dividing the distance between adjacent probes by time to a fraction of probe current peak. Table 4 is a calculation of velocity vs $\dot{B}$ probe position for 10% of the peak current for each probe, where the velocities are averaged over 16 shots using the same experimental conditions. We chose 10% of the peak signal for the magnetic field data because it resulted in the lowest standard deviation in the velocity calculations. The corresponding repeatabilities are shown, which varied among

Table 4 Velocity calculated between adjacent $\dot{B}$ probes by dividing relative probe position by relative time to 10% of peak signal

Probe	Velocity, km/s			Error, %
	Experiment	Uncertainty, %	MACH2	
$\dot{B}_{1\theta}$	28.1	±11	15.9	−43
$\dot{B}_{2\theta}$	27.1	±14	31.7	17
$\dot{B}_{3\theta}$	40.1	±19	39.1	−2.5
$\dot{B}_{5\theta}$	43.1	±4.4	42.3	−1.9
$\dot{B}_{6\theta}$	45.0	±7.1	46.2	2.7

Table 5 Velocity calculated between adjacent light pipe probes by dividing relative probe position by relative time to 10% of peak signal

Probe	Time, μs	Velocity, km/s
LP1	1.39	18.3
LP2	4.24	39.3
LP3	6.36	35.6
LP4	7.82	48.0
LP5	10.68	69.6
LP8	13.15	53.3

the probes. The velocity calculated from the first probe differs by 43% between the experiment and two-dimensional model. As the current sheet propagates downstream, the agreement between the two velocities improves markedly (Table 4), and the velocities are within the repeatability limits for the last three probes. The discrepancy between the experimental velocity and MACH2 is related to the observed delay in arrival of the current sheet in the numerical results. As just discussed, this is possibly caused by either an overprediction in the conductivity or ablation rate. Error in the magnetic field measurements could also play a role.

As a consistency check, one can repeat the velocity calculation for the light pipe signals, as given in Table 5. The velocity from light pipe signals is a time-of-flight measurement for the peak signal between each probe. It is assumed that the strongest light pipe signal corresponds to the arrival of the current sheet, which is consistent with observations made by Keck.[43] With this assumption, the current sheet accelerates as a function of time up to nearly 70 km/s near the end of the inner electrode, and then it decelerates to about 53 km/s nearer the accelerator exit. The increase in velocity up to the end of the inner electrode is consistent with the $\dot{B}$ probe data. It would be difficult to make a more quantitative comparison because the probes are not collocated and because the choice of where to mark the arrival of the current sheet in either the $\dot{B}$ or the light pipe signal brings about 10% uncertainty into the velocity calculation.

Two-Dimensional Features in Simulation

We proceed to examine two-dimensional plots of some of the plasma properties. The results to follow in this section are vector and contour plots of current, velocity, density, temperature, and pressure, at 7.5 and 15 μs. The aspect ratio has been stretched to reveal more detail within the computational domain.

The propagation of the current sheet, along with the corresponding velocity of the fluid is shown in Fig. 6. The radial component of the current density dominates, as indicated by the direction of the vectors in the left half of each plot. Toward the leading edge of the current sheet, the velocity ranges from 75 km/s at the anode to about 15 km/s near the cathode. A simple time-of-flight calculation of the current sheet velocity estimates that the bulk motion of the plasma is about 40 km/s, which is consistent with the velocities determined from the $\dot{B}$ probe and light pipe data.

A sizeable amount of material is accelerated with the current sheet (Fig. 5). Following contours of constant density, the plasma at the anode leads the material at the cathode (Fig. 5) following the slight canting of the current sheet as shown in Fig. 6a. High-pressure regions correspond roughly with regions of high density, especially along the cathode. These high-pressure, high-density islands are entrained with the current sheet.

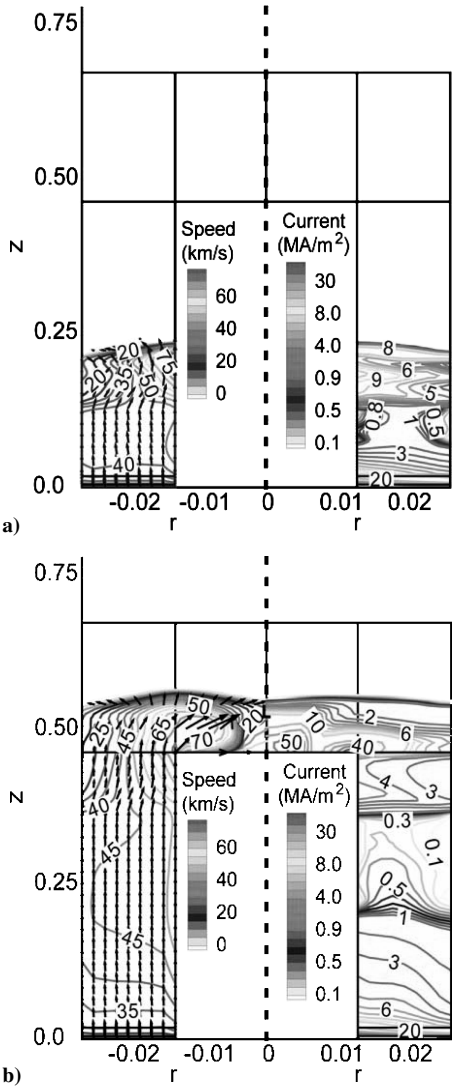

Fig. 6 Simulated speed (left) and current (right) contours at a) 7.5 μs and b) 15 μs. The blocks on the right side of the axis in Fig. 6a are labeled for visual reference for this and subsequent two-dimensional plots.

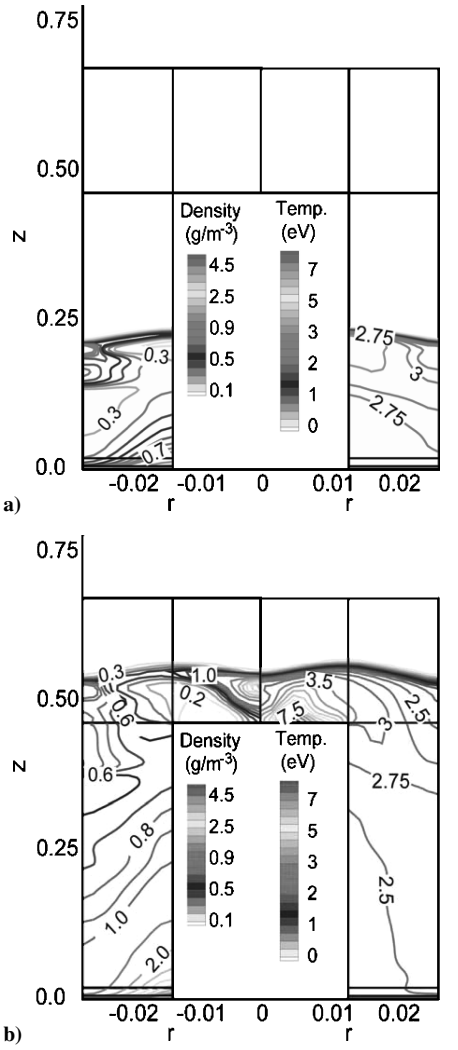

Fig. 7 Simulated density (left) and temperature (right) contours at a) 7.5 μs and b) 15 μs.

The temperature at the leading edge of the current sheet is about 1 to 2 eV (Fig. 7). The temperature is fairly uniform in the interior of the plasma and is typically 2.5 to 3 eV. The plasma heats to 8 eV at the stagnation region downstream of the inner electrode. Ohmic dissipation dominates the heating mechanisms in the model. Radiation is not turned on in the model because of the extreme difficulty in accounting for the line radiation from numerous carbon and fluorine atomic and ionic species present. It is expected that this temperature would be lower if radiation is appropriately modeled.

Of particular interest is the plasma temperature at the breech boundary. The modeling results indicated a temperature of about 1 eV, which is significantly higher than the critical temperature of vaporization of PTFE. This would suggest that the use of the saturated vapor model for ablation and the use of the Clausius–Clayperon equation (3) is not appropriate, and that a model assuming an energy balance in which the ablated material acquires directly the specific enthalpy of the plasma adjacent to the breech boundary to compensate for the thermal transport to the wall would be more appropriate.

On the other hand, the cell temperature calculated by MACH2 is at best an indication of the mean temperature of the computational cell. Depending on the thickness of the ablation boundary layer compared to the thickness of the computational cell, the actual temperature at the surface of the breech insulator could be very different and might well have been significantly lower than the average cell temperature. If the temperature is lower than the critical temperature, then the saturated-vapor model would still apply at the insulator surface. In that case, as the vapor moves away from the insulator surface (but still within the computational cell physically) it is rapidly heated up, leading to an "explosive" flow away from the surface, resulting in a large ablation rate. The latter scenario is implicit in the ablation model used in the present calculation. More diagnostics data are required to throw further light on the ablation process. A first-principle model would properly treat the two cases of temperature and provide a seamless transition from one case to the other, together with a much more refined discretization of the boundary cells to account for the proper energy and momentum transport. This can be pursued in future work. The value of the present modeling results lies in providing insight into these processes and, above all, in indicating the necessity for more diagnostics in future experiments in estimating the density and temperature in the breech region and the amount of ablated mass.

One of the significant discrepancies between the experimental magnetic field probe data and the model is the delayed arrival of the current sheet. We ran three additional cases to test the effects of prefill density and ablation rate by comparison of the magnetic field probe measurements with the baseline case just discussed above, and these are summarized in Table 6. In case 2, we reduced the prefill density by an order of magnitude. In case 3, we artificially lowered the ablation rate by reducing the vaporization densities in Table 3 by an order of magnitude by multiplying the data by an

Table 6 Summary of cases to test effects of ablation rate and prefill density on current measurements[a]

Case	Vapor density coefficient	Prefill density, kg/m^3
1	1.0	1.5×10^{-4}
2	1.0	***1.5 × 10^{-5}***
3	***0.1***	1.5×10^{-4}
4	***0.1***	***1.5 × 10^{-5}***

[a]Parameters that are italicized and in bold are different from the baseline run, case 1.

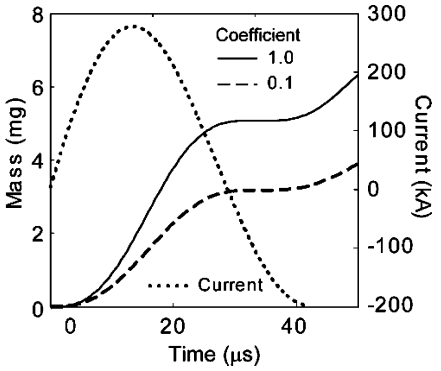

Fig. 8 Ablated mass as a function of time for vapor density coefficients of 1.0 and 0.1. The current is plotted on the right axis for reference.

vapor density coefficient. Case 4 used the reduced prefill density and the reduced vapor density of case 3.

The initial prefill density had a negligible effect on the total ablated mass because the ablation rate in the model depends on the pressure at the breech boundary. After a few time steps the pressure from the ablated plasma is much higher than the cold, prefill gas. Consequently, the rate of mass ablation was a function of time and the vapor density coefficient and independent of the prefill density for the cases investigated. With reference to Fig. 8, the ablation rate (slope of ablated mass curve) is steepest when the current is highest. Although the scope of this study is a numerical investigation of the first quarter pulse of the circuit to capture the current sheet and plasma evolution along the length of the accelerator channel ($\sim$20 μs), the ablation rate is shown to be significant even after the current peak. The total mass ablated by the time the leading edge of the plasma reaches the exit is about 2.2 and 1.4 mg at 15 μs for the vapor density coefficients of 1.0 and 0.1, respectively. About three times the mass is ablated and exhausts more slowly over the 50-μs simulation time.

Even though the vapor density coefficients differed by an order of magnitude, the mass ablated did not. In this ablation model, a reduction of the plasma acceleration at the breech goes as $-\nabla P_{\text{tot}}/\rho$, thereby reducing the vaporization density results in an increase velocity away from the breech, somewhat offsetting the effect vapor density coefficient in determining the net ablation rate.

Regardless of whether or not the insensitivity of the ablation rate is a numerical artifact of the model, the main focus in this section was to attempt to determine if the ablation rate and/or prefill density were too high, causing the discrepancy between the initial propagation of the current sheet in the model and experiment. In all of the runs, the qualitative picture was the same, namely, that the current sheet was delayed in the model compared with the experimental value. However, in cases 2 and 4, when the initial prefill density was reduced, the lag between the magnetic field probe nearest the breech in the model and experiment was only 0.8 μs, compared to 1.8 μs in cases 1 and 3, independent of the vapor density coefficients investigated. This reflects the actual experimental condition of not using a prefilled bore. Thus, there is relatively little mass in the initial plasma, and the initial current sheet propagation in the accelerator depends only on the initial conditions in the accelerator channel.

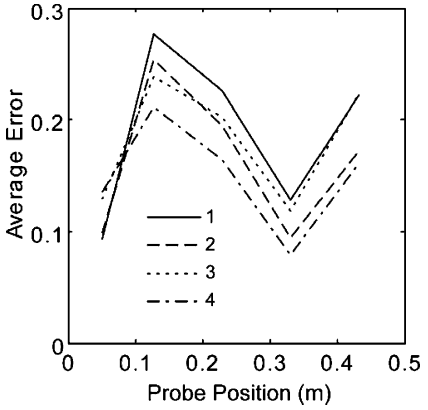

Fig. 9 Average error in magnetic field measurements as a function of probe position.

To quantify the comparisons, we define the relative error of each magnetic field probe current between the experiment and a numerical run at a particular instance in time as

$$\varepsilon_{\text{run},B_{n\theta}}(t) = \frac{\left|I_{\text{exp},B_{n\theta}}(t) - I_{\text{MACH2},B_{n\theta}}(t)\right|}{I_{\text{exp},B_{n\theta},\max}} \tag{5}$$

where the relative errors are calculated at each time step. We plot the time average of each of the relative errors determined with Eq. (5) in Fig. 9. Comparing with the nominal case 1, with the prefill density reduced an order of magnitude (case 2), the relative error is reduced from about 28 to 25% for probes near the breech and from 14 to 9% for probes near the exit, giving an improvement ranging from 10 to 30% in the calculation of the magnetic field. By reducing the vapor density coefficient by an order of magnitude but keeping the prefill density the same (case 3), the relative error in the magnetic field calculations is worse by about 30% at the first probe but improves by as much as 10% for all of the probes downstream. Again, except for the first probe where the relative error is worse by about 30%, the combined reduction of the prefilled density and vapor density coefficient by a factor of 10 (case 4) results in greatly reducing the average discrepancy between the modeling and the experimental results for all of the probes downstream and for the probe at 33 cm by as much as 45%. These results reveal an interesting trend that warrants further investigation.

In the present study (with case 1), the total plasma mass is about 1 mg at about 40 km/s, for an impulse bit of approximately 4×10^{-2} N$\cdot$s. We developed a separate zero-dimensional code based on an arbitrary combination of the "slug" and "snowplow" approaches to assist in the experiments and modeling efforts of higher-order codes such as MACH2. Details from that effort are reported elsewhere.[27–29] Numerical results from the zero-dimensional model gave approximately 0.1 mg of material traveling at 40 km/s, for an impulse bit of 4×10^{-3} N$\cdot$s, about an order of magnitude lower than results from MACH2. The total mass is considerably higher in the two-dimensional model due to the ablating breech boundary, which contributed the majority of the material to the accelerator. Without thrust stand measurements, it is impossible to say which model more accurately represents the thruster performance. Nevertheless, it should be about an order of magnitude higher than typical pulsed plasma thrusters.

Conclusions

The detailed and accurate understanding of the plasma dynamics in pulsed plasma thrusters holds the key toward extending their capabilities in a number of applications, including their applications as high-power (>100-kW) thrusters. For this study, we assessed the behavior and capabilities of MACH2 with a new tabular equation-of-state model for PTFE in modeling the current sheet dynamics in a $\sim$10-kJ pulsed coaxial plasma accelerator with an ablative breech insulator (PTFE). We performed this study in order to improve the code's modeling capabilities and extend the existing application

database of the code. We provided detailed interpretation of the experimental data, based on the two-dimensional results.

First, we compared experimental data of magnetic field probe data in a high-power pulsed plasma thruster using MACH2. We found that the time of arrival current sheet in the model agreed to within 2–3% compared with the downstream magnetic field probes. However, the error was 17–43% on the two probes nearest the breech.

We examined the two-dimensional behavior of the plasma dynamics in the numerical model in more detail, following the qualitative validation of the numerical results with experimental magnetic field probe measurements. The plasma velocity varies from 75 km/s at the anode (inner electrode) to 15 km/s at the cathode, but the bulk motion of the plasma is about 40 km/s. In the acceleration region, the plasma does not typically exceed 3 eV except downstream of the inner electrode. In the model, the conductivity is very high near the breech, trapping the magnetic flux and limiting the acceleration force downstream. This is likely the main source of the discrepancy between the magnetic field probe data in the experiment and model.

These discrepancies were found to be sensitive to the initial prefill density used in the model. Lowering this density an order of magnitude in the model increased the initial propagation speed of the current sheet near the breech, improving agreement with the experimental data at the first probe. Accuracy improved downstream when either the vapor density coefficient in the saturated vapor ablation model or the prefill density were lowered.

In summary, the MACH2 code with the tabular equation of state for PTFE and existing saturated vapor ablation model was able to accurately predict current sheet velocity sufficiently downstream from the breech. The model achieved qualitative agreement of the current sheet distribution and magnetic field strength at various probe positions, within about 20% of experimental data. Current sheet propagation near the breech was not captured successfully. The analysis revealed the importance of boundary and initial conditions on early current sheet evolution near the breech. Future studies using the preceding numerical approach in modeling high-power ablative-fed PPTs should include a first-principle ablation rate model with a refined grid near the breech in combination with more diagnostics to estimate the density, temperature, impulse bit, and ablated mass.

Acknowledgments

We would like to thank Richard Eskridge for his major role in development of the pulsed power laboratory at NASA Marshall Space Flight Center. We would also like to thank Adam Martin, Mike Lee, James Smith, Jeff Richeson, and Doug Davenport for their contributions as well. Work done by Jason Cassibry was supported by the NASA Graduate Student Research Fellowship Program and the Propulsion Research Initiative at the Propulsion Research Center at the University of Alabama in Huntsville.

References

[1]Burton, R. L., and Turchi, P. J., "Pulsed Plasma Thruster," *Journal of Propulsion and Power*, Vol. 14, No. 5, 1998, pp. 716–735.

[2]Filliben, J. D., "Electric Thruster Systems," Chemical Propulsion Information Agency, CPTR 97-65, Columbia, MD, June 1997.

[3]Turchi, P. J., "Directions for Improving PPT Performance," *Proceedings of the 25th International Electric Propulsion Conference*, Vol. 1, The Electric Rocket Propulsion Society, Worthington, OH, 1997, pp. 251–258.

[4]Keefer, D. R., and Rhodes, R., "Electromagnetic Acceleration in Pulsed Plasma Thrusters," *Proceedings of the 25th International Electric Propulsion Conference*, Vol. 1, The Electric Rocket Propulsion Society, Worthington, OH, 1997, pp. 229–236.

[5]Peterkin, R. E. J., Frese, M. H., and Sovinec, C. R., "Transport of Magnetic Flux in an Arbitrary Coordinate ALE Code," *Journal of Computational Physics*, Vol. 140, No. 1998, pp. 148–171.

[6]Peterkin, R. E. J., and Frese, M. H., *MACH: A Reference Manual*, 1st ed., Air Force Research Lab., Phillips Research Site, Kirtland AFB, NM, 1998.

[7]Frese, M. H., "MACH2: A Two-Dimensional Magnetohydrodynamic Simulation Code for Complex Experimental Configurations," Mission Research Corp., AMRC-R-874, Albuquerque, NM, Sept. 1987.

[8]Frese, M. H., "MACH2: A Two-Dimensional Magnetohydrodynamic Simulation Code for Complex Experimental Configurations," NumerEX, Technical Rept. 90-01, Kirtland AFB, NM, 1 March 1990.

[9]Rhodes, R., and Keefer, D. R., "Numerical Simulation of Cableguns Using MACH2," *IEEE Transactions on Plasma Science*, Vol. 31, No. 2, 2003, pp. 248–255.

[10]Spanjers, G. G., Lotspeich, J. S., McFall, K. A., and Spores, R. A., "Propellant Losses Because of Particulate Emission in a Pulsed Plasma Thruster," *Journal of Propulsion and Power*, Vol. 14, No. 4, 1998, pp. 554–558.

[11]Turchi, P. J., Mikellides, I. G., Mikellides, P. G., and Kamhawi, H., "Optimization of Pulsed Plasma Thrusters for Microsatellite Propulsion," AIAA Paper 99-2301, June 1999.

[12]Turchi, P. J., Mikellides, I. G., Mikellides, P. G., and Schmahl, C. S., "Theoretical Investigation of Pulsed Plasma Thrusters," AIAA Paper 98-3807, July 1998.

[13]Shen, Z.-G., Liu, C.-H., Lee, C.-H., Wu, C., and Yang, S., "A Study of a Coaxial Plasma Gun," *Journal of Physics D: Applied Physics*, Vol. 28, No. 2, 1995, pp. 314–318.

[14]Rosenbluth, M. N., "Infinite Conductivity Theory of the Pinch," LA-1850, Los Alamos National Lab., Los Alamos, NM, Sept. 1954.

[15]Andrenucci, M., Caprili, M., and Lazzeretti, R., "Theoretical Models for Plasma Motion in Pulsed Coaxial Hydromagnetic Guns," AGARD, CP-104, June 1972.

[16]Mikellides, P. G., "A Theoretical Investigation of Magnetoplasmadynamic Thrusters," Ph.D. Dissertation, Dept. of Aeronautical and Astronautical Engineering, Ohio State Univ., Columbus, OH, 1994.

[17]Sankaran, K., Choueiri, E. Y., and Jardin, S. C., "Application of a New Numerical Solver to the Simulation of MPD Flows," AIAA Paper 2000-3537, July 2000.

[18]Sankaran, K., Martinelli, L., Jardin, S. C., and Choueiri, E. Y., "A Flux-Limited Numerical Method for Solving the MHD Equations to Simulate Propulsive Plasma Flows," *International Journal for Numerical Methods in Engineering*, Vol. 53, No. 6, 2002, pp. 1415–1432.

[19]Mikellides, P. G., and Turchi, P. J., "Applied-Field Magnetoplasmadynamic Thrusters, Part 2: Analytic Expressions for Thrust and Voltage," *Journal of Propulsion and Power*, Vol. 16, No. 5, 2000, pp. 894–901.

[20]Mikellides, P. G., Turchi, P. J., and Roderick, N. F., "Applied-Field Magnetoplasmadynamic Thrusters, Part 1: Numerical Simulations Using the MACH2 Code," *Journal of Propulsion and Power*, Vol. 16, No. 5, 2000, pp. 887–893.

[21]Mikellides, P. G., Turchi, P. J., and Roderick, N. F., "Analysis of Applied-Field Plasma Thrusters Using the Mach2 Code," AIAA Paper 94-3338, June 1994.

[22]Mikellides, P. G., Turchi, P. J., and Roderick, N. F., "Theoretical Model for Applied-Field MPD Thrusters," AIAA Paper 95-2676, July 1995.

[23]Mikellides, P. G., Turchi, P. J., and Mikellides, I. G., "Design of a Fusion Propulsion System-Part 1: Gigawatt-Level Magnetoplasmadynamic Source," *Journal of Propulsion and Power*, Vol. 18, No. 1, 2002, pp. 146–151.

[24]Markusic, T. E., Choueiri, E. Y., and Berkery, J. W., "Measurements of Current Sheet Canting in a Pulsed Electromagnetic Accelerator," *Physics of Plasmas*, Vol. 11, No. 10, 2004, pp. 4847–4858.

[25]Cheng, D. Y., "Application of a Deflagration Plasma Gun as a Space Propulsion Thruster," *AIAA Journal*, Vol. 9, No. 9, 1971, pp. 1681–1685.

[26]Ziemer, J. K., "Performance Scaling of Gas-Fed Pulsed Plasma Thrusters," Ph.D. Dissertation, Dept. of Mechanical and Aerospace Engineering, Princeton Univ., Princeton, NJ, Feb. 2001.

[27]Cassibry, J. T., "Numerical Modeling Studies of a Coaxial Plasma Accelerator as a Standoff Driver for Magnetized Target Fusion," Ph.D. Dissertation, Dept. of Mechanical and Aerospace Engineering, Univ. of Alabama, Huntsville, AL, Sept.–Oct. 2004.

[28]Thio, Y. C. F., Eskridge, R., Lee, M., Smith, J. W., Martin, A. K., Markusic, T. E., and Cassibry, J. T., "An Experimental Study of a Pulsed Electromagnetic Plasma Accelerator," AIAA Paper 2002-4269, July 2002.

[29]Thio, Y. C. F., Cassibry, J. T., and Wu, S. T., "2-D Magnetohydrodynamic Modeling of a Pulsed Plasma Thruster," AIAA Paper 2002-2194, May 2002.

[30]Guman, W. J., "Pulsed Plasma Technology in Microthrusters," Air Force Aero Propulsion Lab., AFAPL-TR-68-132, Wright–Patterson AFB, OH, Nov. 1968.

[31]Palumbo, D. J., and Guman, W. J., "Effects of Propellant and Electrode Geometry on Pulsed Ablative Plasma Thruster Performance," AIAA Paper 75-409, March 1975.

[32]Mikellides, P. G., and Neilly, C., "Pulsed Inductive Thruster, Part 1: Modeling, Validation and Performance Analysis," AIAA Paper 2004-4091, July 2004.

[33]Mikellides, P. G., "Modeling and Analysis of a Megawatt-Class Magnetoplasmadynamic Thruster," *Journal of Propulsion and Power*, Vol. 20, No. 2, 2004, pp. 204–209.

[34]Schumer, J. W., Swanekamp, S. B., Ottinger, P. F., Commisso, R. J., Weber, B. V., Smithe, D. N., and Ludeking, L. D., "MHD-to-PIC Transition for Modeling of Conduction and Opening in a Plasma Opening Switch," *IEEE Transactions on Plasma Science*, Vol. 29, No. 3, 2001, pp. 479–493.

[35]Mikellides, P. G., and Turchi, P. J., "Modeling of Late-Time Ablation in Teflon Pulsed Plasma Thrusters," AIAA Paper 96-2733, July 1996.

[36]Peterkin, R. E. J., Degnan, J. H., Hussey, T. W., Roderick, N. F., and Turchi, P. J., "A Long Conduction Time Compact Torus Plasma Opening Switch," *IEEE Transactions on Plasma Science*, Vol. 21, No. 5, 1993, pp. 522–527.

[37]Peterkin, R. E. J., "Compact Toroid Simulations with MACH2," Mission Research Corp., MRC/ABQ-R-1130, Albuquerque, NM, Dec. 1988.

[38]Braginskii, S. I., "Transport Processes in a Plasma," *Reviews of Plasma Physics*, Vol. 1, edited by M. A. Leontovich, Consultants Bureau, New York, 1965, pp. 205–311.

[39]Spitzer, L., Jr., *Physics of Fully Ionized Gases*, 2nd ed., Interscience, New York, 1962.

[40]Vincenti, W. G., and Kruger, C. H. J., *Introduction to Physical Gas Dynamics*, Wiley, New York, 1965, Chaps. 3–5.

[41]Wentink, T., Jr., "High Temperature Behavior of Teflon," Avco-Everett Research Lab. Div., AVCO Corp., AFBMD-TN-59-15, Everett, MA, July 1959.

[42]Coleman, H. W., and Steele, W. G., *Experimentation and Uncertainty Analysis for Engineers*, 2nd ed., Wiley, New York, 1999, Chap. 2.

[43]Keck, J., "Current Speed in a Magnetic Annular Shock Tube," *The Physics of Fluids Supplement*, Vol. 7, No. 11, 1964, pp. S16–S27.